Study of Lateral Flow in a Stratified Tidal Channel-Shoal System
The Importance of Intratidal Salinity Variation

Zhou, Zaiyang; Ge, Jianzhong ; Wang, Zhengbing ; van Maren, Bas; Ma, Jianfei; Ding, Ping Xing

DOI
10.1029/2019JC015307

Publication date
2019

Document Version
Accepted author manuscript

Published in
Journal Of Geophysical Research-Oceans

Study of lateral flow in a stratified tidal channel-shoal system: the importance of intra-tidal salinity variation

Zaiyang Zhou[1,2], Jianzhong Ge[1,3*], Zheng Bing Wang[2,4], D.S. van Maren[2,4], Jianfei Ma[1], Pingxing Ding[1]

[1]State Key Laboratory of Estuarine and Coastal Research, East China Normal University, Shanghai, China, 200062
[2]Faculty of Civil Engineering and Geosciences, Delft University of Technology, 2628 CN Delft, The Netherlands
[3]Institute of Eco-Chongming (IEC)，No.20 Cuiniao Road, ChenJiazhen, Shanghai, China, 202162
[4]Deltares, 2600 MH Delft, The Netherlands

Corresponding author: Dr. Jianzhong Ge (jzge@sklec.ecnu.edu.cn)

Key Points:

- Intra-tidal salinity variation (ISV) and a strong lateral flow in a channel-shoal system were identified by an integrated tripod system.
- A 3D hydrodynamic model has been developed to analyze the relationship between ISV and the lateral flow, revealing that lateral flows were primarily driven by the salinity-induced pressure gradient.
- Lateral flows can be generated or enhanced by human interventions such as groyne fields.

Abstract

Lateral flow significantly contributes to the near-bottom mass transport of salinity in a channel-shoal system. In this study, an integrated tripod system was deployed in the transition zone of a channel-shoal system of the Changjiang Estuary (CE), China, to observe the near-bottom physics with high temporal/spatial resolution, particularly focusing on the lateral-flow-induced mass transport. These in-situ observations revealed a small-scale salinity fluctuation around low water slack during moderate and spring tidal conditions. A simultaneous strong lateral current was also observed, which was responsible for this small-scale fluctuation. A high-resolution unstructured-grid Finite-Volume Community Ocean Model (FVCOM) has been applied for the CE to better understand the mechanism of this lateral flow and its impact on salinity transport. The model results indicate that a significant southward near-bed shoal-to-channel current is generated by the salinity-driven baroclinic pressure gradient. This lateral current affects the salinity transport pattern and the residual current in the cross-channel direction. Cross-channel residual current shows a two-layer structure in the vertical, especially in the intermediate tide when the lateral flow notably occurred. Both observation and model results indicate that near-bottom residual transport of water moved consistently southward (shoal to channel). Mechanisms for this intra-tidal salinity variation (ISV) and its implications can be extended to other estuaries with similar channel-shoal features.

1 Introduction

As transition zones between riverine and marine environments, estuaries experience a wide range of physical, chemical and biological processes, e.g. suspended material transport, chemical reaction of dissolved ions, variation of biological productivity. These processes influence not only ecology but also have socio-economic impacts because many large cities are located in the vicinity of estuaries (Woodroffe et al., 2006).

Salinity is a significant driver for sediment trapping, e.g. sediment accumulation at the front of salt wedge where the convergence of fresh and saline water occurs (Postma, 1967). The upstream limit of salt intrusion is an indicator for location of estuary turbidity maximum (Dyer, 1986), the dynamics of which in itself strongly influences the navigability. Moreover, salinity also has an effect on ecology, e.g. its impact on temporal distribution of planktons (Dube et al., 2010).

The long-term, large-scale salt balance is primarily the result of landward transport by estuarine circulation and tidal dispersion (Bowen, 2003; Fischer, 1976) balancing seaward transport by riverine residual flow (Dronkers, 2018). These salt transport mechanisms depend on the longitudinal salinity gradient and (in combination with hydrodynamic mixing) give rise to vertical salinity gradients. Vertical salinity gradients may cause salinity stratification which controls the intensity of momentum exchanges from the surface to the bottom (Simpson et al., 1990).

In addition to these longitudinal and vertical processes, lateral processes in estuaries also have effects on mass transport. Cross-channel (lateral) currents are relatively small (about 10% in magnitude) compared to the along-channel currents (Lerczak & Geyer, 2004). However, their influences on dynamics of estuaries may be significant by generating considerable cross-channel gradients in salt, turbidity and other constituents.

Lerczak & Geyer (2004) set up a model for an idealized straight estuary. Their results suggest that lateral circulation is stronger during flood tides than ebb tides. This asymmetry is caused by the interaction between lateral circulation, stratification and differential advection by along-channel tidal currents. The flood-ebb asymmetry of lateral flow patterns may lead to an asymmetric cross-sectional shape of a straight channel. However, in a channel which already is asymmetrically shaped, lateral flow will also be affected by bathymetric features, as well as hydraulic structures. Huijts et al. (2006) studied the mechanisms for lateral sediment entrapment using an idealized model. They examined mechanisms that could lead to the sediment accumulation, including Coriolis forcing and lateral density gradients. They found that because of the difference of along-channel flow velocity from bed to surface, the intensity of the Coriolis deflection varies from bed to surface. Therefore, vertical circulation in the lateral direction can be induced by the Coriolis deflection. Fugate et al. (2007) conducted an observation in upper Chesapeake Bay, USA, focusing on the impact of lateral dynamics on sediment transport. Using a lateral momentum balance they observed that stronger cross-channel circulation by rotational effects (Coriolis and channel curvature) is larger during the ebb. A modelling study by Zhu et al. (2018) in a strongly anthropogenically impacted estuary (the Changjiang Estuary) suggest that lateral circulations are strong near the main navigation channel, and peak close to slack tide conditions. This has great implications for siltation rates in the channel, in which more than 80 million m^3/year (by 2011) needs to be dredged annually (Wang et al., 2015). This fuels a great interest in the dynamics of lateral flows in general, but in the CE in particular.

Cross-sectional flows influence the salinity, leading to an intra-tidal salinity variation (ISV). Many studies have identified the salinity's response to the longitudinal and vertical process (Bowen, 2003; Dronkers, 2018; Dyer, 1986; Simpson et al., 1990). However, few observations directly relate salinity fluctuations to lateral flows. Yet, salinity variations may provide an indicator for lateral flows, which is much easier to measure than transverse flows themselves. The objective of this study is to detect evidence for lateral flow using a combination of flow velocity and salinity observations, and quantitatively analyze and explain their driving mechanisms and effects. This paper is organized as follows. Section 2 introduces the study area, methods for observation and data analysis, and the numerical model. Section 3 presents the main results of observations and simulations, focusing on formation of ISV and the mechanism for the lateral flow. Section 4 gives discussion on momentum balance, stratification and mixing, effects of dikes and groynes and the implication of ISV. Main conclusions are summarized in section 5.

2 Study site, observational and numerical method

2.1 Study site

Field observations were carried out in one of the four outlets of the CE (Fig. 1). The discharge of the Changjiang River, measured at the Datong Gauging Station, is approximately 40000 m^3/s in wet season, about 10000 m^3/s in dry season. The mean and maximum tidal ranges are approximately 2.7 m and 4.6 m, respectively, measured at Zhongjun Gauging Station.

The CE is characterized as a channel-shoal system with multiple outlets and shallow shoals. The South Channel (SC), North Passage (NP) and South Passage (SP) are the major tidal channels in the turbidity maximum zone of the CE. The NP is deepened and protected, resulting in the so-called Deepwater Navigation Channel (DNC), aiming at improving the shipping capacity in and out of the CE. The protection works include two 50 km long dikes parallel to the flow, to which 19 groynes perpendicular to the flow are attached (Fig. 1).

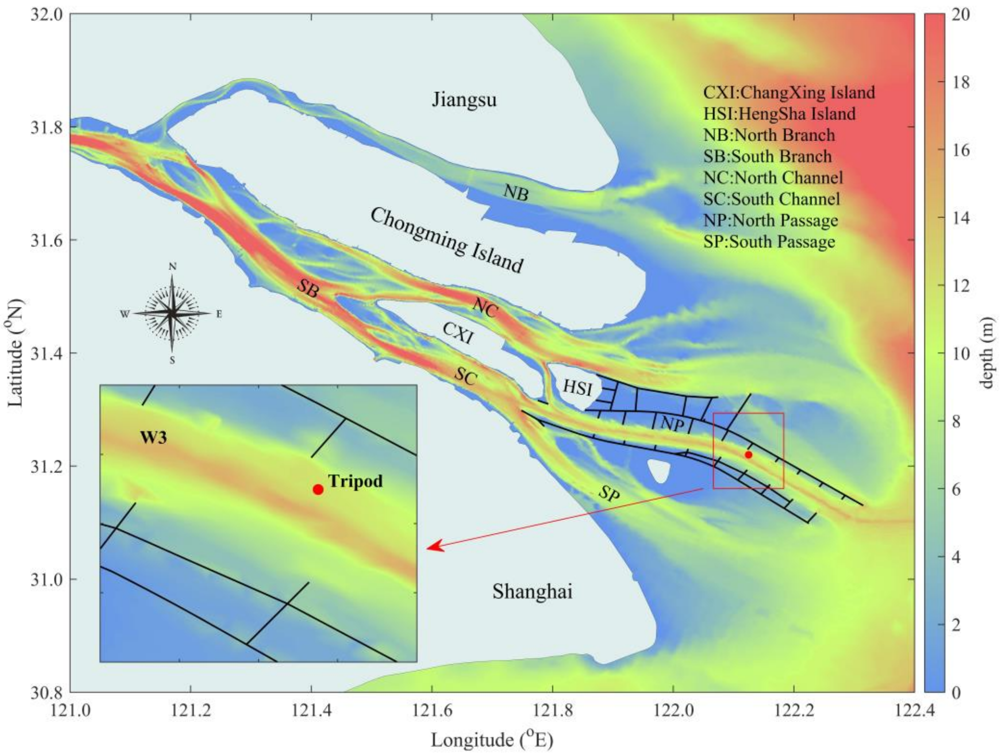

Figure 1: Bathymetry of the Changjiang Estuary and adjacent regions. The black lines in the river mouth indicate dikes and groynes around the North Passage. The red dot indicates the measuring site. W3 is the bending corner of the main channel.

The estuarine turbidity maximum of the CE is located in the North Passage (NP), resulting in strong sedimentation rates (Ge et al., 2015, 2018; Liu et al., 2011). Many groynes have been buried since the construction of the DNC. This has led to shallow shoals in the groyne region and a deeper main channel in the middle of the NP, forming a typical channel-shoal system. Cross-channel flows have been observed in the NP through observational and numerical studies (Liu et al., 2011; Zhu et al., 2018). The NP is also the main mixing front of freshwater and saline water, resulting in strong horizontal salinity gradient and vertical stratification (Ge et al., 2012, 2018; Wu et al., 2012).

2.2 Observation methods

The middle section of the NP, located in the center of the turbidity maximum, was selected to conduct our observations (red rectangle in Fig. 1). A tripod system was deployed on the north side of the main channel, an area with pronounced saltwater intrusion and a strongly stratified water column (Ge et al., 2018). The observation site was in the middle of the shallow shoal and the main channel to observe lateral flows between the shoal and the deep channel.

The tripod system was designed to measure flow velocity and direction, salinity, suspended sediment concentration and temperature near the bottom. To achieve this goal, the tripod integrated multiple instruments (Fig. 2). An upward-looking 600 kHz RDI Acoustic Doppler Current Profilers (ADCP-up) was mounted 1.2 m above the sea bed (abbreviated as ‘mab’) with a resolution of 0.5 m for each cell. A downward-looking 1200 kHz RDI ADCP (ADCP-down) was placed 1.03 mab to measure velocities from 0.2 to 0.7 mab at high resolution (0.1 m) near the bed. Based on earlier observations (Liu et al., 2011), the ADCP with 1200 kHz sensor frequency works well in the near-bottom area under typical high sediment concentration for this area. A Nortek Acoustic Doppler Vector was mounted at 0.4 mab to measure the near-bed current velocities at a sampling frequency of 16 Hz, which means valid data were collected at the height of about 0.25 mab. The tripod system also included a Point Current Meter (ALEC, JFE ALEC CO., LTD, JAPAN) at 1.45 mab to obtain flow velocities in the blanking range of ADCP-up, a Tide/wave Logger (RBR, RBR Ltd., Canada) at 1.0 mab to record wave conditions and a Conductivity, Temperature, and Pressure Recorder (CTD, Sea-Bird Electronics, Inc., USA) at 1.0 mab to record temperature and salinity continuously. An Optical Backscattering Sensor (OBS, D&A Instruments CO, type: 3A, USA) was also fixed to the side edge of the tripod. Detailed configurations of instruments installed on the tripod such as burst interval, sampling duration and sampling frequency are listed in Table. 1.

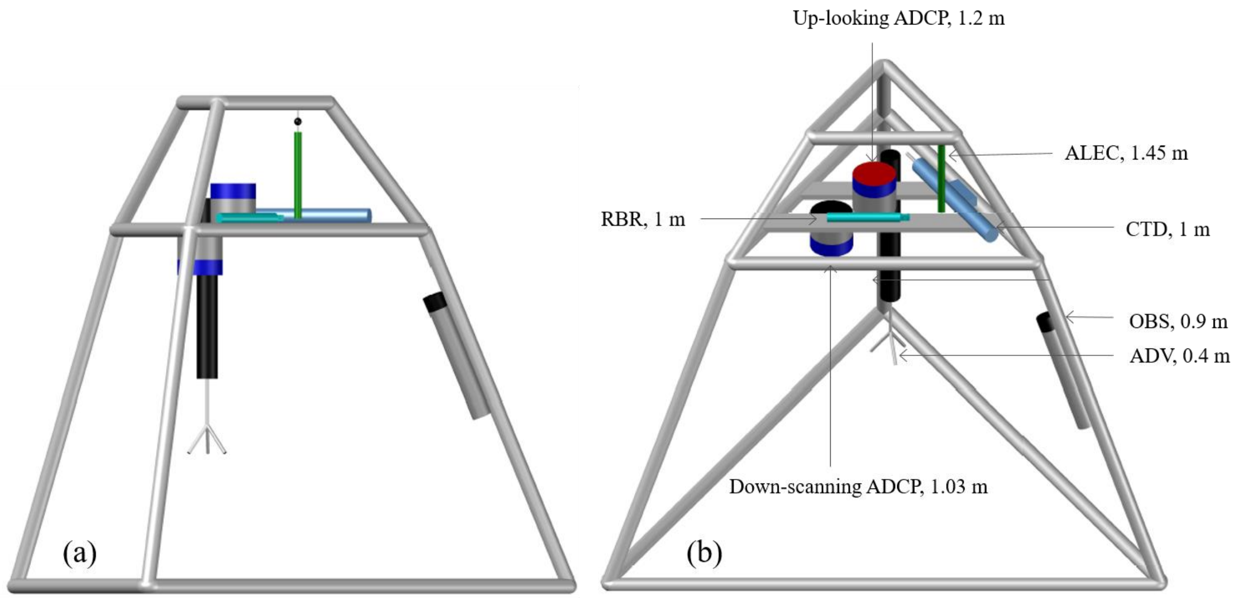

Figure 2: Side-view and top-view of the tripod system.

Table 1: Instruments mounted on the tripod and their sampling configurations.

Instrument deployed	Distance above bed (m)	Sampling interval (min)	Sampling configuration	Survey parameter
ADCP-up	1.2	/	120s	Profile velocity
ADCP-down	1.03 (down)	/	120s	Profile velocity
ADV	0.25	10	16Hz (every first 70s)	Near-bed velocity
RBR	1	10	4Hz	Wave conditions
ALEC	1.45	2	0.2Hz (every first 50s)	Velocity
OBS	0.9	/	100s	Salinity, temperature, turbidity, pressure
CTD	1	/	120s	Salinity, temperature, pressure

The tripod was deployed on December 6, 2016 (abbreviated as 12/06), in the dry season of the year. The observations lasted for about 12 days, and the tripod was recovered on 12/18, 2016. The 12 days covered a whole period from the neap tide to the spring tide. The neap tide was from 12/07 to 12/09, and the spring tide was on 12/14 - 12/16.

2.3 Numerical Model

To resolve the irregular geometries of the channel, shoals and submerged/exposed dikes and groynes, a hydrodynamic numerical model based on the Finite-Volume Community Ocean Model has been applied for the CE (CE-FVCOM). FVCOM is a three-dimension, unstructured-grid coastal ocean model. A triangle mesh is used horizontally, and σ-coordinates in the vertical. A generalized dike-groyne module is implemented in FVCOM to resolve submerged and exposed man-made coastal and offshore engineering works (Ge et al., 2012). Previous observations showed that the water column in the NP is occasionally strongly salinity stratified, and opposite flows form a two-layer flow structure in the vertical (Ge et al., 2013, 2018). As a mode split model, the adjustment between 3-D internal mode and 2-D external mode could be problematic for capturing this two-layer flow structure (Lai et al., 2010). Therefore, we use a semi-implicit scheme which is capable of well simulating the two-layer-structure flows.

The geographically unstructured mesh of FVCOM covers the whole CE as well as the inner shelf of the East China Sea, Hangzhou Bay, and Zhoushan Archipelago (Fig. 3). Different from the original mesh configuration (Ge et al., 2012, 2013), the river boundary in this model is extended to ~ 600 km upstream Datong Gauging Station to better resolve the river-estuary interaction (Fig. 3a). It provides flexible resolution from the open boundary in the inner shelf to channels and shoals at the river mouth. The horizontal resolution of this model is down to ~200 m in the channel (Fig. 3b).

The model is forced by 8 major astronomical tidal constituents specified at the open boundaries, including four diurnal tides (K_1, O_1, P_1 and Q_1), four semi-diurnal tides (M_2, S_2, N_2 and K_2). The data for the tidal constituent sources are from TPXO 8 (Egbert & Erofeeva, 2002). Daily river discharge of the CJ (data source: www.cjh.com.cn) is considered at the upstream boundary at Datong Gauging Station. The atmospheric forcing is the ERA-Interim data from the European Centre for Medium-Range Weather Forecasts (ECMWF) with 0.125° spatial resolution and 3-hour temporal resolution. This model is discretized into 20 uniform terrain-following sigma layers, which provides sufficient vertical resolution for the bathymetry of 5 - 13 m in this channel-shoal system. The time step is set to 10 seconds with a spin-up time of 15 days. For the turbulence scheme, a Mellor and Yamada level-2.5 turbulent closure scheme with Galperin modification is applied (Chen et al., 2003; Galperin et al., 1988; Mellor & Yamada, 1982). The horizontal and vertical Prandtl number defined as the ratio of turbulent eddy viscosity to the turbulent diffusivity (Chen et al., 2013), are 1.0 and 0.4 respectively.

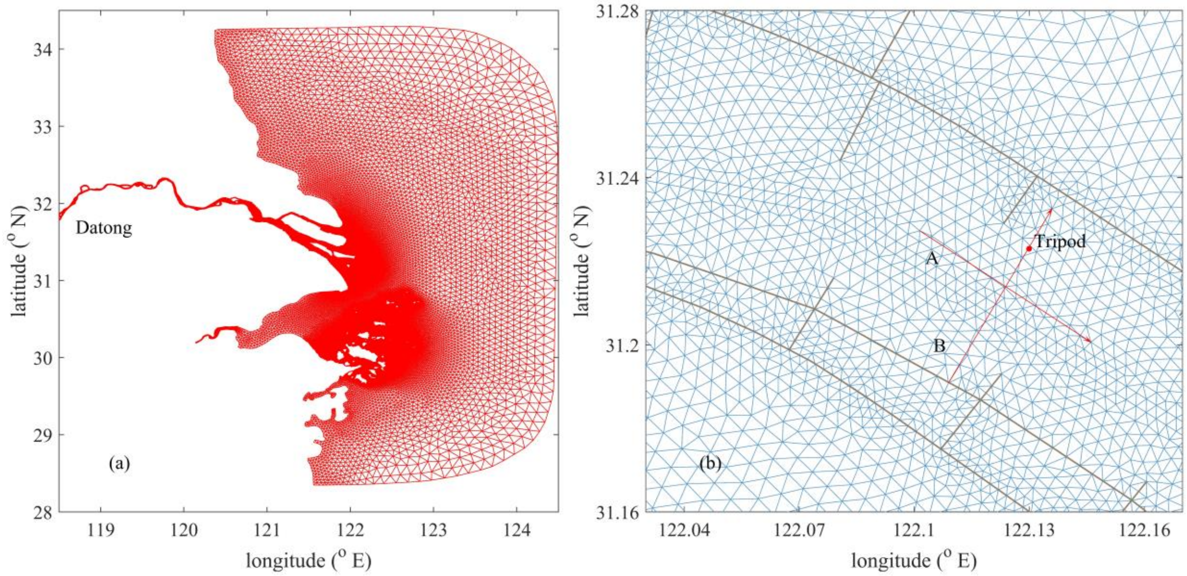

Figure 3: (a) Unstructured mesh for the Changjiang Estuary and adjacent regions. (b) An enlarged view within the NP. Section A, B is selected along- and cross-channel sections for analysis.

3 Results

3.1 General physics (flow velocity, salinity)

The main data measured by various instruments of the tripod, including water levels, fixed-point velocity and salinity are shown in Fig. 4. The whole observation period can be divided into three phases according to the tidal condition: Phase A from 12/07 to 12/11 (neap tidal conditions), Phase B from 12/11 to 12/14 (intermediate tidal conditions) and Phase C from 12/14 to 12/18 (spring tidal conditions).

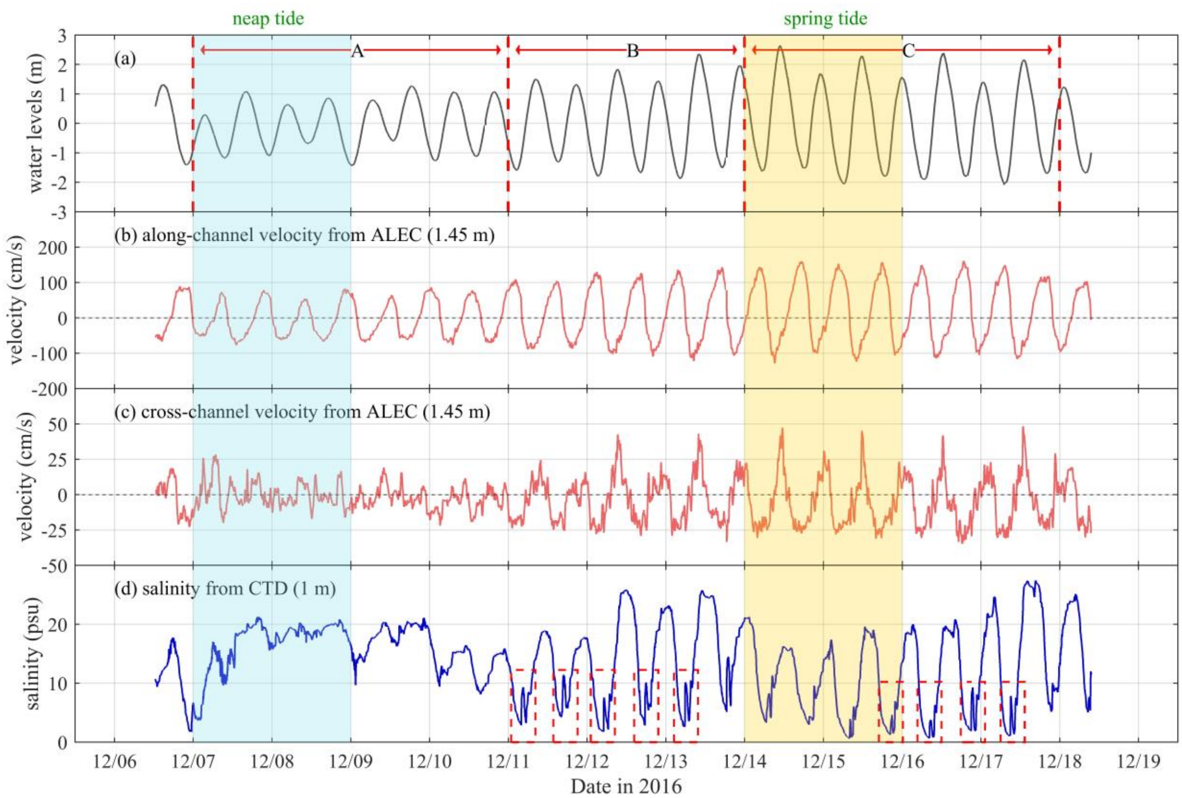

Figure 4: Time series of (a) water levels, (b) horizontal along-channel and (c) cross-channel velocity from ALEC, (d) water salinity from CTD by the tripod. An orthogonal coordinate according to channel direction is used for velocity decomposition. For along-channel flow, the positive value indicates direction of about 120 degrees from the north, for cross-channel flow, the positive value indicates direction of about 30 degrees from the north.

The tidal range during neap tides was ~2 m, and increased to ~4 m during spring tides (Fig. 4a). The average bottom current velocity at 1.45 mab during neap tides was 44.5 cm/s, and almost double during spring tides, reaching 86.1cm/s (Fig. 4b, c). The maximum current velocity exceeded 150.0 cm/s during ebb tide. The mean flood duration during neap tides was 7.29 h, whereas the mean ebb duration was 5.25 h.

The cross-channel velocity component was irregular during neap tides (Fig. 4c) with weak-amplitude fluctuation. The maximum cross-channel velocity during neap tides is ~25 cm/s (06:45 LST on 12/07). During intermediate and spring tidal conditions, the cross-channel velocity had a pronounced flow asymmetry. During intermediate tides, southward cross-channel flow occurred for 57% of time (with the remaining 43% northward flow), increasing to 68% of time during spring tides. Also the average strength of southward flow was greater: 15.1 cm/s during intermediate tides and 17.0 cm/s during spring tides (11.6 cm/s and 15.6 cm/s for northward flow for the respective tidal conditions). Consequently, there is a pronounced (shoal-to-channel) cross-channel velocity component, both in magnitude and duration, resulting from lateral flows.

The bottom salinity remained above ~20.0 PSU for several days with only small oscillations during neap tides. This indicates that the area remains in the range of the salt wedge during neap tides, as observed earlier by Ge et al., (2018). During intermediate and spring tidal conditions, an oscillating salinity pattern can be observed, with values ranging from nearly 0 PSU around the low water slack to 30 PSU around the high water slack (Fig. 4d). In addition, from 12/11 to 12/18 (phases B and C), a series of significant oscillations lasting for about 2 hours with magnitude of about 5 PSU occurred in each trough of salinity curve (Fig. 4d). We refer to these oscillations as intra-tidal salinity variations (ISV), and will be elaborated on in more detail in the next section.

3.2 Identification of intra-tidal salinity variation (ISV)

The ISVs were highly consistent with the tidal phase, always occurring during low water slack (marked by red rectangles in Fig. 4d). During an ISV, the salinity first increases for about 20 minutes, and then drops for about 51 minutes (averaged value of 5 ISVs during intermediate tides). Although the ISVs were identified during intermediate and spring tidal conditions, the amplitude was larger and the duration was longer during intermediate tides. The ISVs disappeared shortly before saline flood currents entered the North Passage close to the observation area. During this period, the upper water column was dominated by ebb currents while the bottom area was dominated by flood currents (Fig. 5e, h). This typical two-layer current structure occurred during low water slack, with weak currents in the whole water column. Importantly, during a period when ISVs occurred (green dashed lines in Fig. 5f, i), the flow direction was ~210 degrees from the north (Fig. 5e, h).

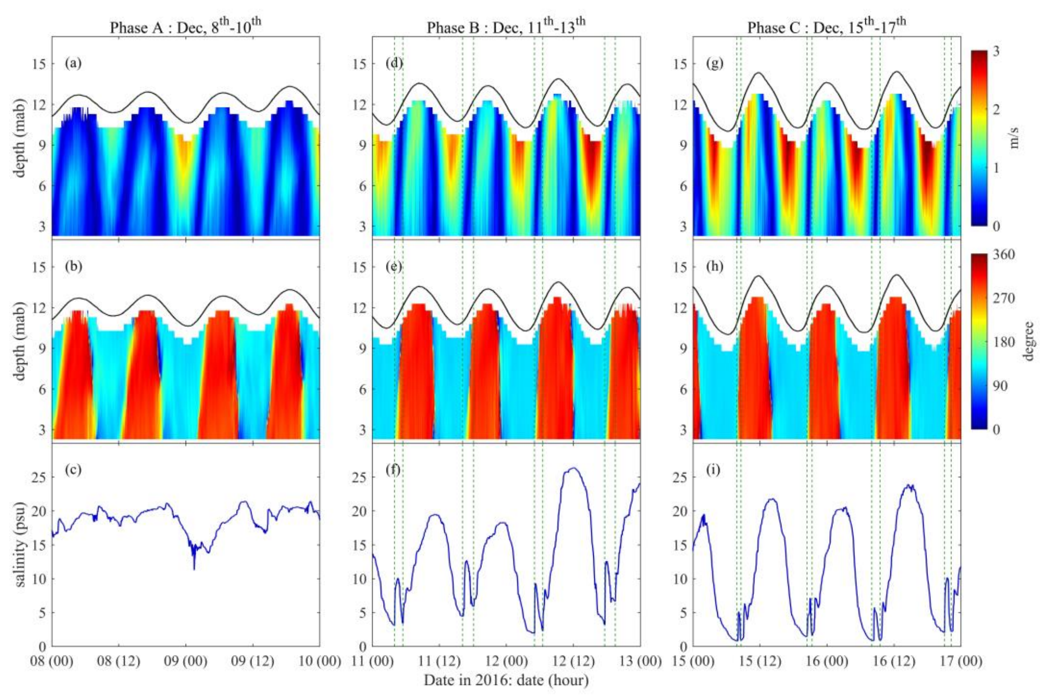

Figure 5: Time series of vertical profiles of flow velocity (row 1), flow direction (row 2), near-bed salinity (row3) during neap tides (left column), intermediate tides (middle column) and spring tides (right column). The green dashed lines mark the occurrence of ISVs.

The observation indicates the formation of ISV is related to lateral flows. However, this measurement only demonstrates the ISV in a local perspective. It is unable to resolve the horizontal and vertical propagation of the water and salinity mass under the effect of the lateral flow. Therefore, the mechanism for the formation of ISV needs to be examined with a numerical model, allowing a more detailed quantitative analysis of the lateral flows.

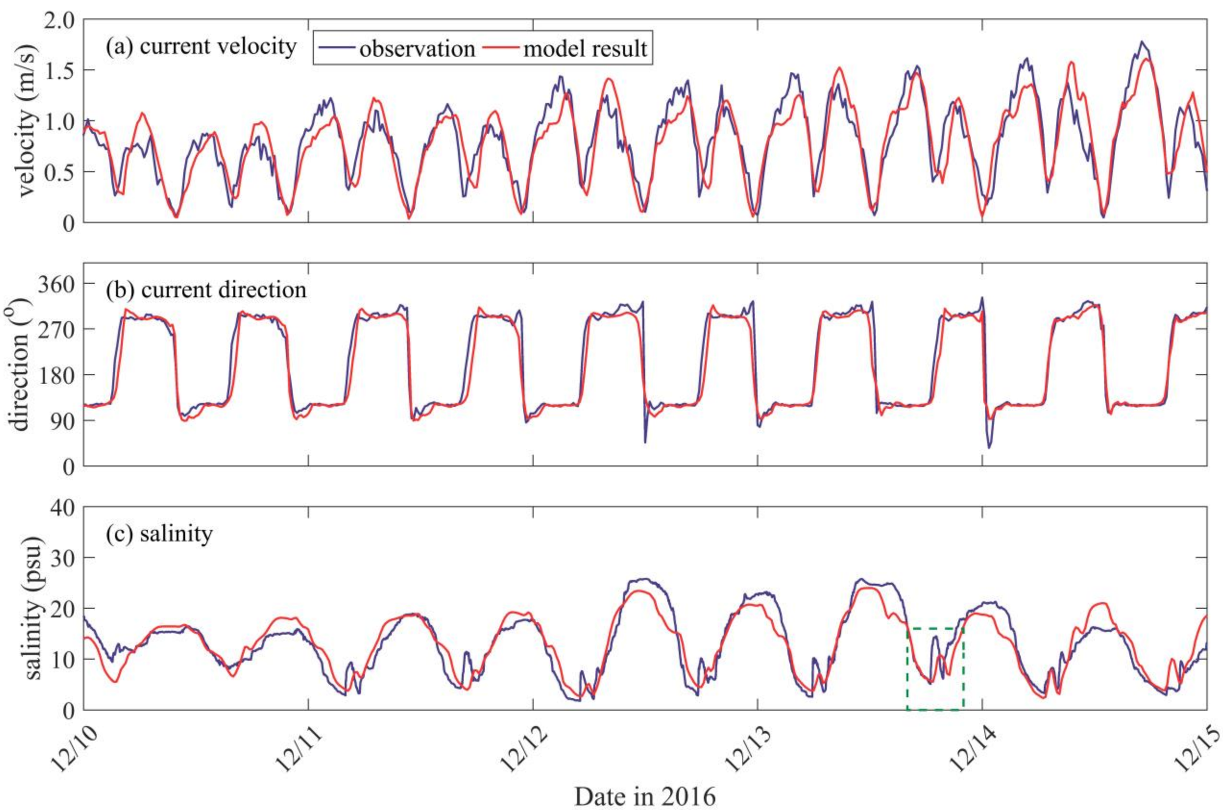

Figure 6: Model-data comparison between observed (blue) and simulated (red) results for near-bed tide current velocity (a), current direction (b) and salinity (c) at the observation site. The green dashed rectangle in (c) shows a typical intra-tidal salinity variation (ISV), and this ISV will be discussed in details in the following sections.

The applied model (CE-FVCOM) has been fully validated against hydrodynamics, tide, salinity in previous studies (Ge et al., 2012, 2013, 2014, 2015; Guo et al., 2018). In this study, model results are only compared to our tripod data for further validation. A comparison of near-bed flow velocity, direction and salinity (shown in Fig. 6) shows that the model captures the magnitude and direction of the upward-looking ADCP (data of the first cell, 2 mab), and the variation of salinity collected by CTD. The overall root mean square errors (RMSEs) for velocity magnitude, velocity direction and salinity are 0.19 m/s, 15.1 degrees and 2.6 PSU, respectively. Even more, the ISVs occurring during intermediate and spring tidal conditions are also well resolved by the model (an example is marked with green dashed box in Fig. 6c). Since the model predicts the occurrence and correct timing of the ISVs, the model can be used to further explore formation mechanisms in more detail.

3.3 Formation and breakdown of the ISV

To understand the formation and breakdown of ISV, a typical ISV during neap-to-spring transition tides is selected (marked by a green dashed rectangle in Fig. 6c) for analysis with the numerical model. At the end of ebb, the salinity in the channel (including the observation site, Fig. 7a) was low while the shoals are more saline. The higher salinity on the shoals generates a near-bed salinity-driven density current peaking at 0.5 m/s (Fig. 8e, f). The transport of more saline water from the shoals towards the channel leads to an increase in near-bed salinity (Fig 7a-c), giving rise to the formation of ISV.

The amount of saline water stored over the shoals is limited, however. The high-salinity patch flows 1.5 km into the channel (Fig. 8f, g) after which it dilutes or is advected up-estuary (Fig. 8g-i). During the period of maximum cross-channel flow (Fig. 8e), the near-surface ebb currents are close to 1 m/s (Fig. 9e). Such a large velocity gives rise to mixing, which is illustrated with the local salinity distribution. Near the observation point, the near-surface salinity increases (Fig. 9f-h) when the near-bed salinity decreases (Fig. 8f-h, 9f-h). The salinity rapidly rises after flow reversal when the saline flood propagates into the channel (Fig. 9i, Fig. 7e, f).

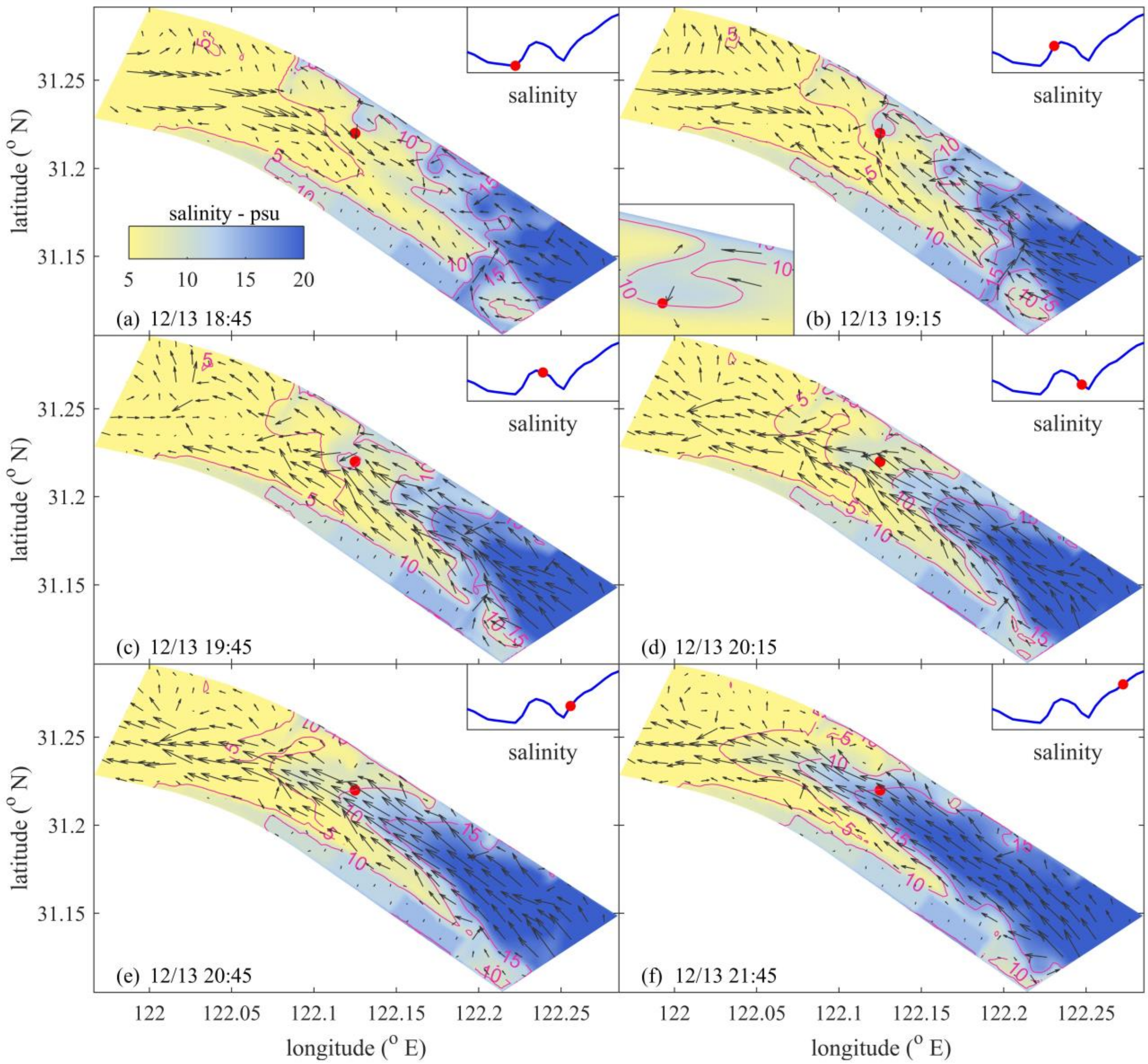

Figure 7: Spatial distributions of near-bed salinity and flow velocity at selected times (model result). The red dot indicates the observation site. The up-right inset shows the process of ISV and the red dot shows salinity of the site during this typical ISV period.

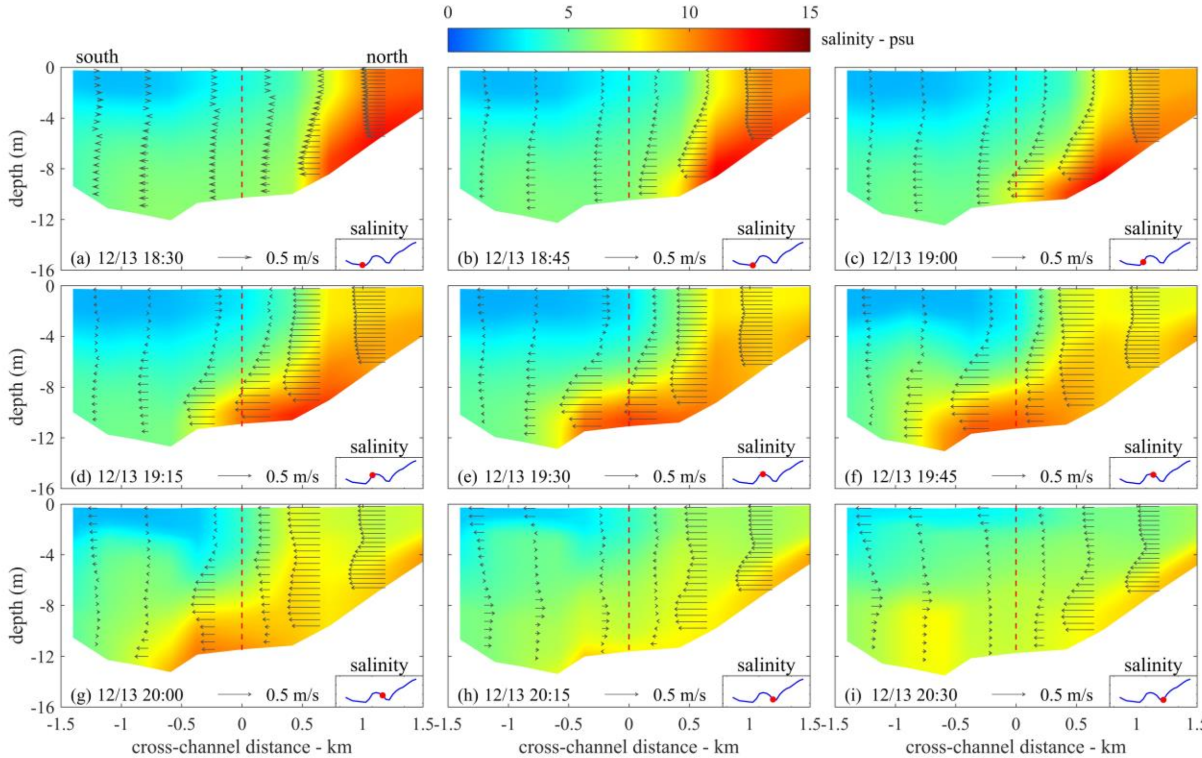

Figure 8: Vertical distribution of salinity and cross-channel flow velocity (arrows) at selected times (a typical intra-tidal salinity variation period). Red dashed line indicates the projection position of the observation site in a south-north cross-channel section (section B in Fig. 3b). The down-right insets show the process of ISV and the red dot shows salinity of the site during this typical ISV period.

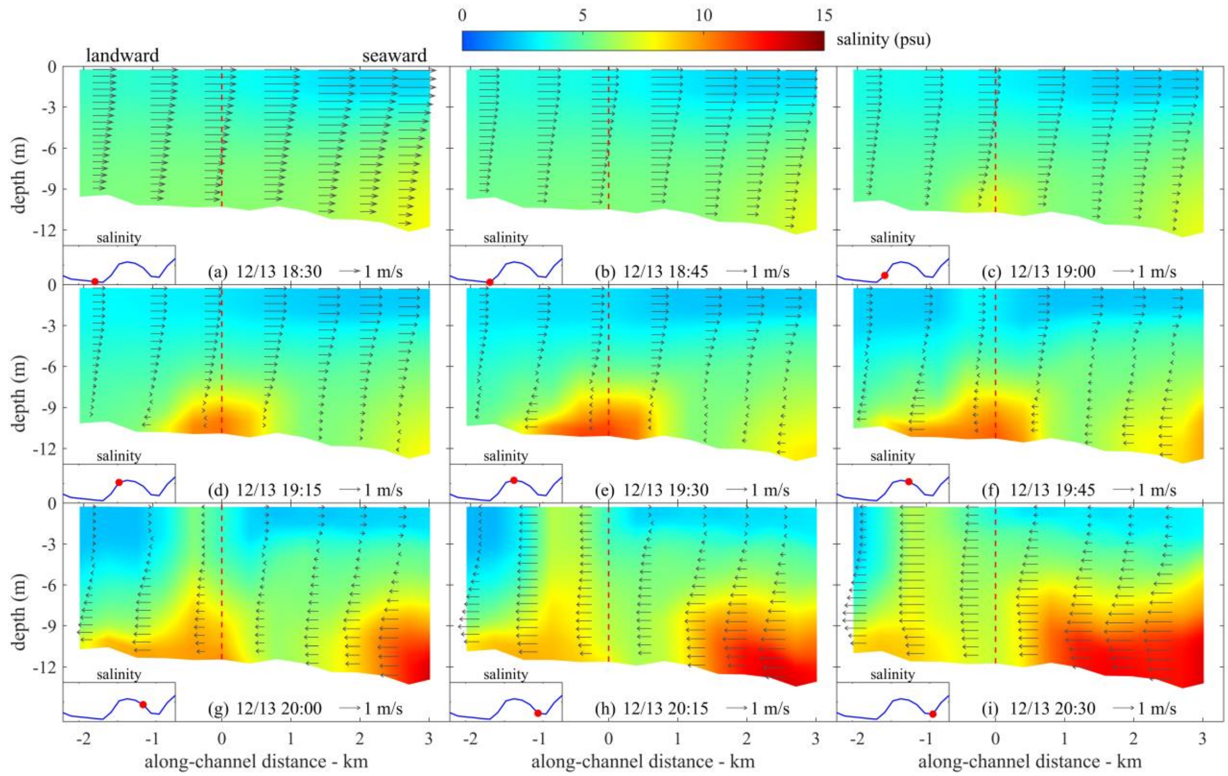

Figure 9: Vertical distribution of salinity and along-channel flow velocity (arrows) at selected times (a typical intra-tidal salinity variation period). Red dashed line indicates the projection position of the observation site in a west-east along-channel section (section A in Fig. 3b). The down-left inset shows the process of ISV and the red dot shows salinity of the site during this typical ISV period.

Averaged over the tide, the lateral flows discussed above contribute to a tide-averaged cross-channel residual current (Fig. 10). The variation of this tidally averaged cross-current over the spring-neap tidal cycle can be evaluated with the upward-looking ADCP observations. During the late neap tide and the intermediate tide when pronounced ISV was detected, the cross-channel residual current showed a clear vertical variability (Fig. 10a, b). For the majority of time, the tidally averaged cross-channel component near the bed is directed towards the channel whereas it is directed towards the shoals near the water surface.

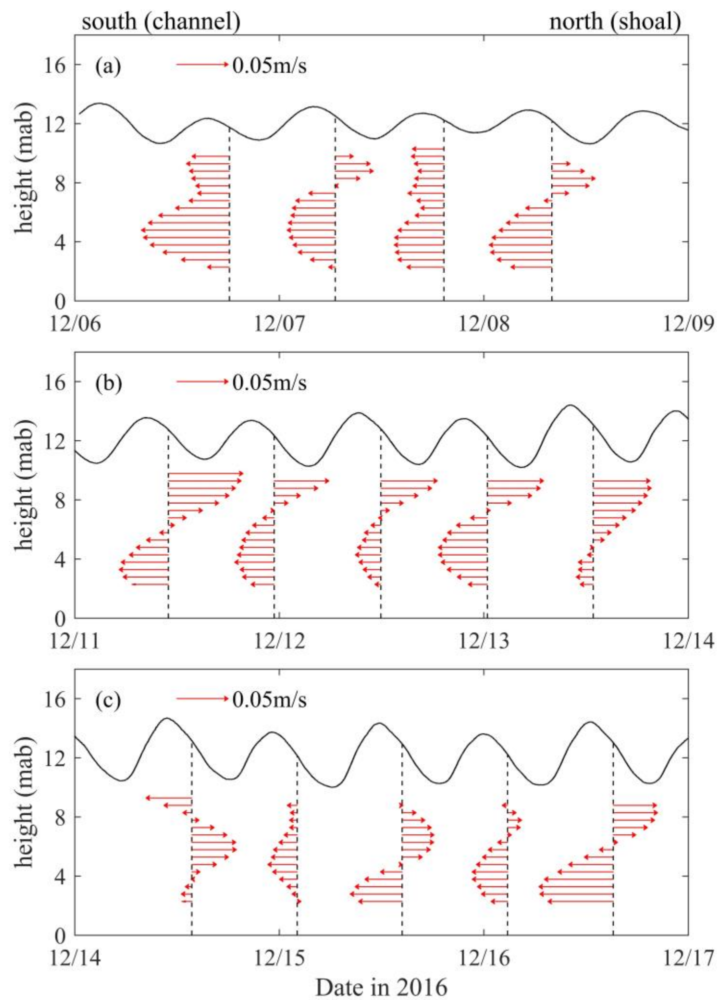

Figure 10: Tidally averaged cross-channel residual current calculated from ADCP results in (a) neap tide, (b) intermediate tide and (c) spring tide at the observation site.

4 Discussion

4.1 Mechanism for the lateral flow: momentum balance analysis

Interpretation of the data and numerical model results suggests that the density-induced gradient resulting from the salinity difference between the channel and the shoal is the driving force for the lateral flow. We will further quantify this hypothesis using a momentum balance analysis.

We define the along-channel direction as the x-axis (the positive value indicates a direction of 120 degrees from the north) and the cross-channel direction as the y-axis (the positive value indicates a direction of 30 degrees from the north, away from the main channel), over which the governing equations for horizontal motions are given as follows:

$$\underbrace{\frac{\partial u}{\partial t}}_{A}+\underbrace{u\frac{\partial u}{\partial x}+v\frac{\partial u}{\partial y}+w\frac{\partial u}{\partial z}}_{B}\underbrace{-fv}_{C}=\underbrace{-\frac{1}{\rho}\frac{\partial(P_H+P_a)}{\partial x}}_{D}+\underbrace{\frac{\partial}{\partial z}\left(K_m\frac{\partial u}{\partial z}\right)}_{E}+\underbrace{F_x}_{F} \quad (1)$$

$$\underbrace{\frac{\partial v}{\partial t}}_{A}+\underbrace{u\frac{\partial v}{\partial x}+v\frac{\partial v}{\partial y}+w\frac{\partial v}{\partial z}}_{B}\underbrace{+fu}_{C}=\underbrace{-\frac{1}{\rho}\frac{\partial(P_H+P_a)}{\partial y}}_{D}+\underbrace{\frac{\partial}{\partial z}\left(K_m\frac{\partial v}{\partial z}\right)}_{E}+\underbrace{F_y}_{F} \quad (2)$$

where x, y and z are the horizontal and vertical axes of the Cartesian coordinate; u, v and w are the x-, y-, and z-component velocities, respectively; ρ is density; P_H is hydrostatic pressure; P_a is the air pressure at sea surface; f is the Coriolis parameter and K_m is vertical eddy viscosity coefficient. Here, F_x and F_y represent the horizontal momentum diffusion terms in the along- and cross-channel directions, respectively.

The air pressure is omitted due to its weak contribution to the local hydrodynamics in the channel-shoal system. The hydrostatic pressure P_H satisfies:

$$\frac{\partial P_H}{\partial z}=-\rho g \Rightarrow P_H=\rho_0 g\zeta+g\int_z^0 \rho dz \quad (3)$$

where g is the gravitational acceleration.

In Eqs. (1) and (2), $A-F$ denote the local acceleration, advection, Coriolis force, pressure gradient, and vertical and horizontal momentum diffusion terms, respectively. The pressure gradient force term includes the barotropic (surface elevation) pressure gradient force and baroclinic (density) pressure gradient force as described in Eq. (3).

Figure 11 shows the vertical distribution of momentum terms of the Coriolis force and baroclinic pressure gradient (BPG) along the selected section B at selected times at before (18:30), right on the crest of (19:30) and after (20:15) a significant ISV on 12/13. The BPG was ~ - $3*10^{-4}$ m/s^2 at 18:30 LST 12/13 in the shoal area (Fig. 11d). The Coriolis force was ~ - $4*10^{-5}$ m/s^2, one order of magnitude smaller than the BPG since tidal currents are weak during low water slack (Fig. 11a). The BPG and Coriolis force jointly drove the flow southward (from the north shoal to the main channel), generating the lateral current. In this stage, the BPG was the major contributor among all dynamical forces. At 19:30 LST 12/13, the BPG continued to drive the southward lateral flow, counteracted by the Coriolis force because near bottom this Coriolis force was in the northward direction (Fig. 11b). Similarly, the Coriolis force was one order of magnitude smaller than the BPG. Therefore, this hindrance effect could not substantially inhibit the development of the lateral flow. At the end of the ISV period when flood currents flowed into the channel, and the Coriolis force was in the northward direction in the whole section (Fig. 11c), the BPG in the deep channel increased and had a northward component because of the movement of saline water (Fig. 11f). Later, BPG in the deep channel would continue to increase due to seawater intrusion.

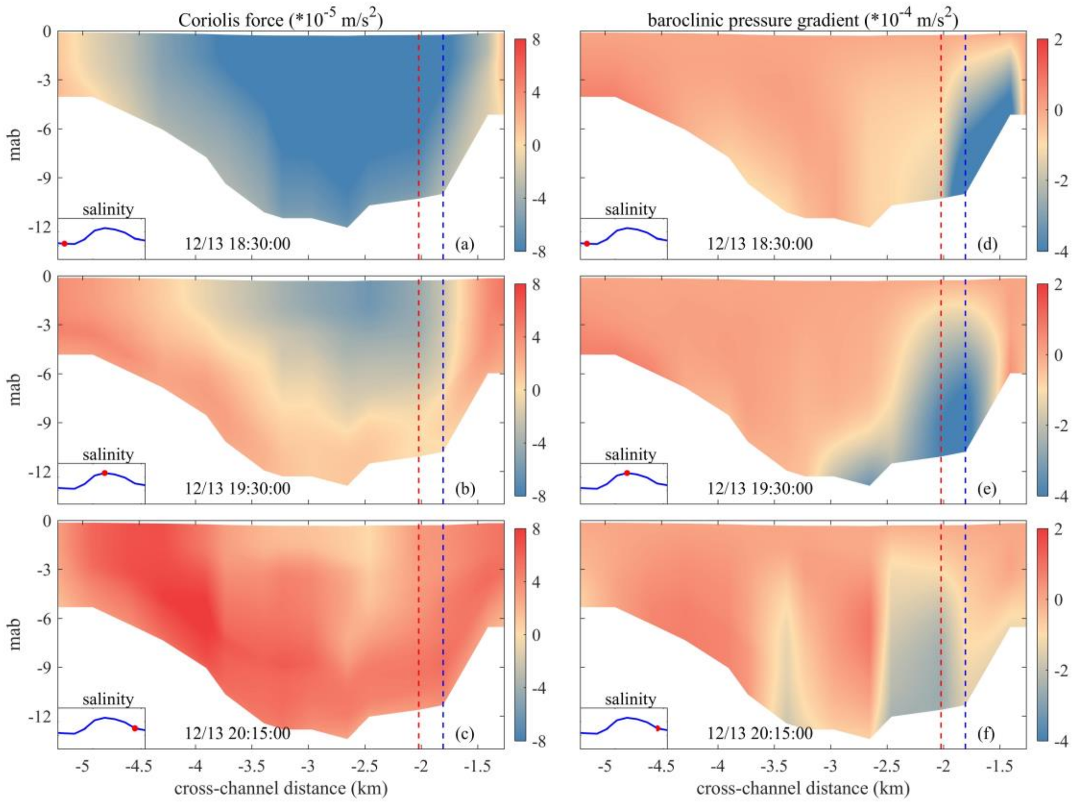

Figure 11: Vertical distributions of Coriolis force (left column) and baroclinic pressure gradient (right column) along the selected cross-channel section B in the intra-tidal salinity variation (ISV) period. The red dashed line indicates the location of the observation site, and the blue dashed line shows an adjacent location north to the site. The down-left inset shows the process of ISV in salinity and the red dot shows salinity of the site during this typical ISV period.

The momentum term due to flow curvature is also estimated. Eqs. (1) and (2) are written in Cartesian coordinate, which do not contain separate momentum term induced by channel curvature. The momentum equation can be written in curvilinear coordinate as follows (Chant, 2010) :

$$\frac{\partial u_n}{\partial t} + u_s \frac{\partial u_n}{\partial s} - \frac{{u_s}^2}{R} + f u_s + g \frac{\partial \eta}{\partial n} - \frac{\partial \tau}{\partial z} = 0 \tag{4}$$

where s, n, z represent main-flow, lateral and vertical directions, u_s, u_n are velocity components in s, n directions, R is the radius of curvature, f is the Coriolis parameter, η is water level, τ is stress. In Eqs. (4), $\frac{{u_s}^2}{R}$ is momentum term of channel curvature, which is also named centrifugal acceleration. The longitude and latitude information of the north dike is transferred into a Cartesian coordinate, using a map projection method. Then the new position of the north dike in the Cartesian coordinate is fitted with a quadratic curve to calculate R. For cross-channel section B (Fig. 3b) which passes the observation site, $R \approx 49.7$ km, maximum magnitude of u_s was about 1.9 m/s (Fig. 5b), thus maximum value of $\frac{{u_s}^2}{R}$ was about 7.3*10^{-5} m/s^2. At the beginning of ISV (18:30 LST 12/13), u_s was about 0.2 m/s, and the effect of channel curvature was several orders of magnitude smaller than that of the BPG. Therefore, the baroclinic pressure gradient caused by the horizontal salinity gradient was the main driving force for the formation of the lateral flow.

Closer to the channel bend (Fig. 1), $R \approx 28$ km, and here curvature effects could be larger. During the ebb tide, the maximum value of $\frac{{u_s}^2}{R}$ is about 1.3*10^{-4} m/s^2, towards the outside of the channel. While the Coriolis force is about - 1.1*10^{-4} m/s^2. These two forces were close and the joint effect is small. However, during the flood tide, maximum centrifugal acceleration is about 1.0*10^{-4} m/s^2 while the Coriolis force is about 1.3*10^{-4} m/s^2. The combined effect of channel curvature and Coriolis force (about 2.3*10^{-4} m/s^2 in total) is comparable to that of the baroclinic pressure gradient which generates the lateral flow. In the other word, this combined effect could also lead to an opposite lateral flow during flood tide period close to the river bend.

Because u_s in the channel curvature term is squared, this term always has the same sign within a whole tidal cycle. It may therefore strengthen or weaken the Coriolis term in different stages of a tidal cycle, giving rise to tidal asymmetry in lateral flows during flood and ebb tide (Chant, 2010). In many cases, lateral flow or lateral circulation could be dominated by the centrifugal acceleration for a period in a tidal cycle (Kim & Voulgaris, 2008; Lacy & Sherwood, 2004; Nidzieko et al., 2009) as the radius of curvature R is much smaller than that in our study. Although R is relatively large and the curvature induced term appear to be less important than other terms, variation of R leads to different lateral circulation patterns in different cross-channel sections of the North Passage. In this study, the maximum joint effect of Coriolis term and centrifugal term is still smaller than the BPG when ISV was generated, indicating the significance of the trapped saline patch in the shallow shoal and the intensity of this lateral flow.

4.2 Stratification and mixing

Differential advection of the water mass leading to ISV greatly influences stratification and mixing process in the channel-shoal system. During the ISV period, the cross-channel and along-channel salinity distribution and velocity showed a pronounced vertical variability (Fig.8, Fig. 9). To what extent feedback mechanisms exist between salinity-induced stratification and the flow is further investigated with the gradient Richardson number (R_i):

$$R_i = -\frac{g}{\rho_w}\frac{\partial\rho/\partial z}{[(\frac{\partial u}{\partial z})^2+(\frac{\partial v}{\partial z})^2]} \tag{5}$$

where ρ_w is water density, $\partial\rho/\partial z$ is density gradient, u, v are velocity components in x-, y-direction. The water column stratifies when R_i exceeds 0.25. Therefore $\log_{10}(Ri/0.25)$ is used as an index for the degree of stratification (Fig. 12, with positive values indicating stratifying conditions). The density of water did not always increase from the surface to the bottom, resulting in negative values of R_i which give rise to the blank areas in Fig.12 when taken as a logarithm. As explained earlier, the saline water remaining in the shallow areas flowed downslope at the end of the ebb due to horizontal density differences, giving rise to the ISV. As a result of this density current, the near-bed channel gradually became more stratified (Fig. 12b, c) by differential advection of salinity. During the peak of the ISV (Fig. 12c), the larger part of the water column was salinity-stratified. However, the layer very close to the bed had a weak stratification (Fig. 12c). This is because of the large gradient of velocity in the near-bed area due to the friction (Fig. 8e).

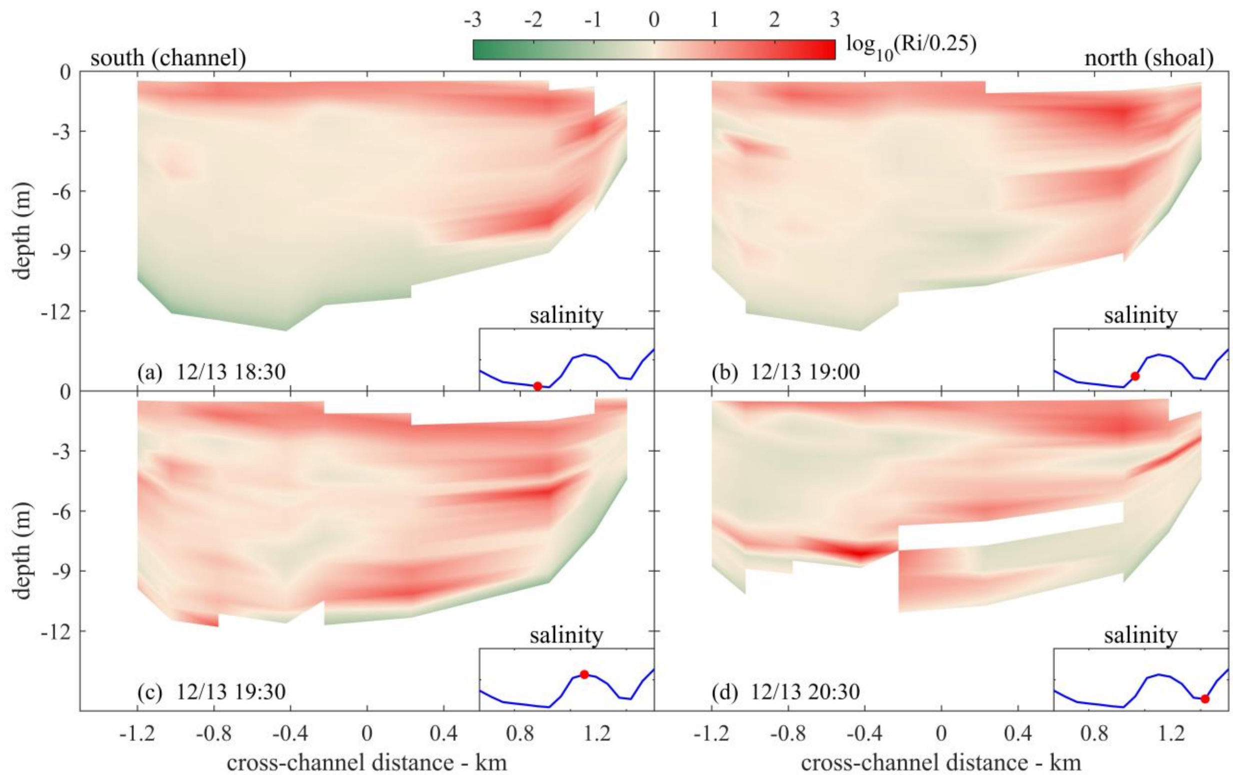

Figure 12. Distribution of $\log_{10}(Ri/0.25)$ in cross-channel section B (a) before the ISV, (b) in the increasing stage of ISV, (c) at the peak of ISV and (d) at the end of the ISV. The zero position in x-axis indicates the position of the observation site in the section. The down-right inset shows variation of salinity, and the time-stamp salinity at the site.

The gradient Richardson number (R_i) indicates the stratification at a specific height in the whole vertical column while the bulk Richardson number (R_{ib}) provides information of the whole water column (bottom to surface). R_{ib} can be calculated as (Hoitink et al., 2011; Lewis, 1997):

$$R_{ib} = \frac{gD\Delta\rho}{\overline{\rho_w}\left|\overrightarrow{u_s}^2\right|} \tag{6}$$

where D is the water depth, $\Delta\rho$ is the density difference between surface and bottom, $\overline{\rho_w}$ is the averaged density of the water column, $\overrightarrow{u_s}$ is the horizontal velocity at the surface. The gradient Richardson number of different layers and the bulk Richardson number are shown in Fig. 13. Turbulent kinetic energy (TKE) per unit mass is also used for further interpretation of vertical mixing. TKE can be calculated using the high-frequency velocity data collected by ADV as:

$$TKE = \frac{1}{2}(\overline{u'^2} + \overline{v'^2} + \overline{w'^2}) \tag{7}$$

Green, blue and red dashed lines in Fig. 13 indicate the start, peak (salinity maximum) and end of the ISV, respectively. Note that Fig. 13a is based on model results while Fig. 13b, 13c are based on results of the tripod observation. Therefore, a small time lag of ISV process between these two methods can be found in Fig. 13 (vertical dashed lines are different in three sub-graphs). Shortly before the start of the ISV (green dashed lines), the near-bottom R_i and R_{ib} were below 0.25 (Fig. 13a), indicating well-mixed condition. Both the time-variation in near-bed salinity ($dsal/dt$, Fig. 13c) and vertical salinity variation (Fig. 8a) were small. All information therefore suggests a steady, well-mixed water column near the end of the ebb. During the first stage of the ISV (between green and blue dashed lines), the salinity and R_{ib} increased rapidly (Fig. 13). R_i at 1.5 mab showed a different variation from R_i at 0.5 and 1.0 mab. At 1.5 mab, there was a pronounced stratification as it was close to the interface between water in the salinity patch and ambient water. During the decreasing stage of the ISV (between blue and red lines), the whole water column (as indicated with the bulk Richardson number) remained stably stratified (R_{ib} > 0.25). The near-bed gradient Richardson numbers suggest a non-stratified water column, but this was because the halocline was located higher up in the water column. The observation that the water column was stratified during the decline of the ISV suggests that longitudinal advection (and not mixing) was the main mechanism responsible for the salinity decrease. Well-mixed conditions (R_{ib} < 0.25) re-established halfway the flood, during periods of high TKE.

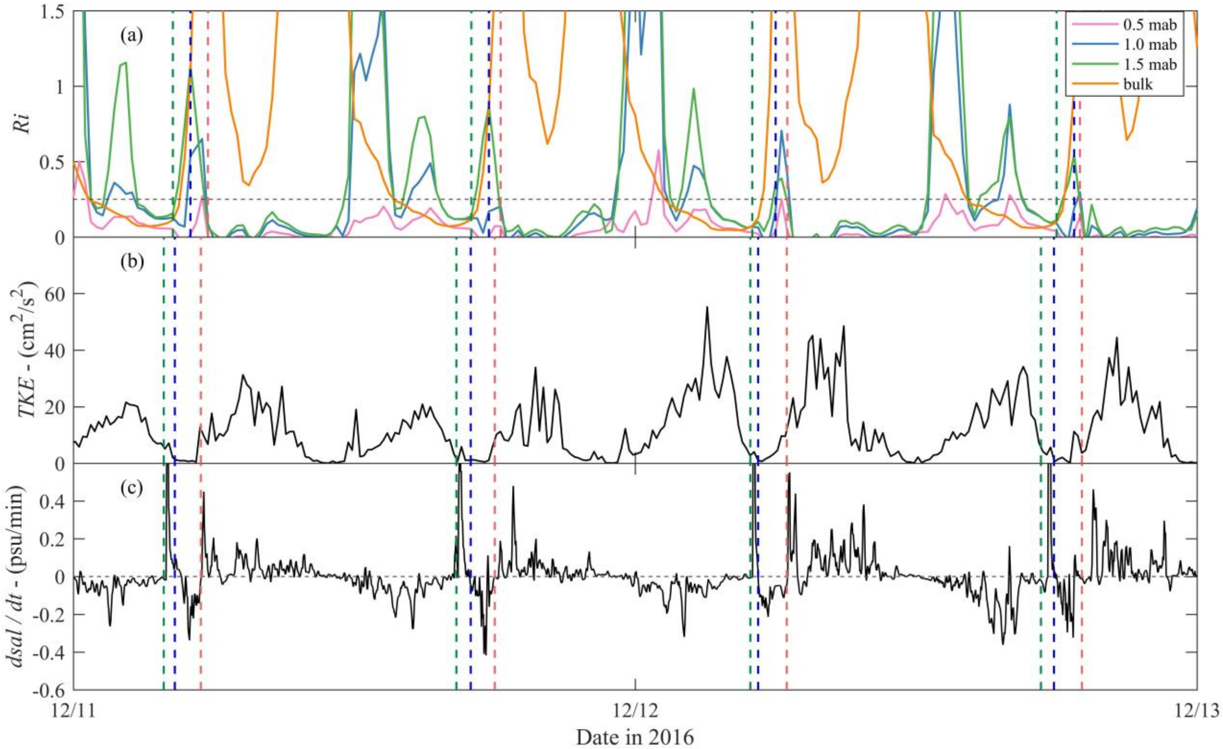

Figure 13: Time series of (a) gradient Richardson number at 0.5 mab (pink), 1.0 mab (blue), 1.5 mab (green) and bulk Richardson number (orange), (b) turbulent kinetic energy (TKE) at the observation site, (c) rate of salinity change in time. Green and blue dashed lines indicate the increasing stage in the ISV, blue and red dashed lines indicate the decreasing stage in the ISV.

4.3 Effects of dikes and groynes

The investigated tidal channel was surrounded both towards the south and north with dikes and overflowing groynes (Fig. 1). Although the main parts of the groynes from the tip are submerged by sediment deposition, the remaining parts near dikes are still exposed during low tide, which shapes the groyne-sheltered area as a semi-enclosed region. The groynes create nearly stagnant water masses, and therefore strengthen differential advection of salt water. As a result, these groynes may greatly contribute to the transverse flows (and therefore ISV).

The effect of groynes is quantified by rerunning the model with one groyne (nearest to the observation site) removed. As a result, the ISV is no longer predicted at the observation site (Fig. 14a). The bottom salinity distribution clearly shows that no high-salinity water is trapped in the north shoal without the groyne (Fig. 14c). This is also clear in vertical salinity distribution in the cross-channel section and cross-channel velocity is much smaller than the original case (Fig. 14e). For downstream areas where groynes are still present, salinity is still influenced by the groynes (Fig. 14c).

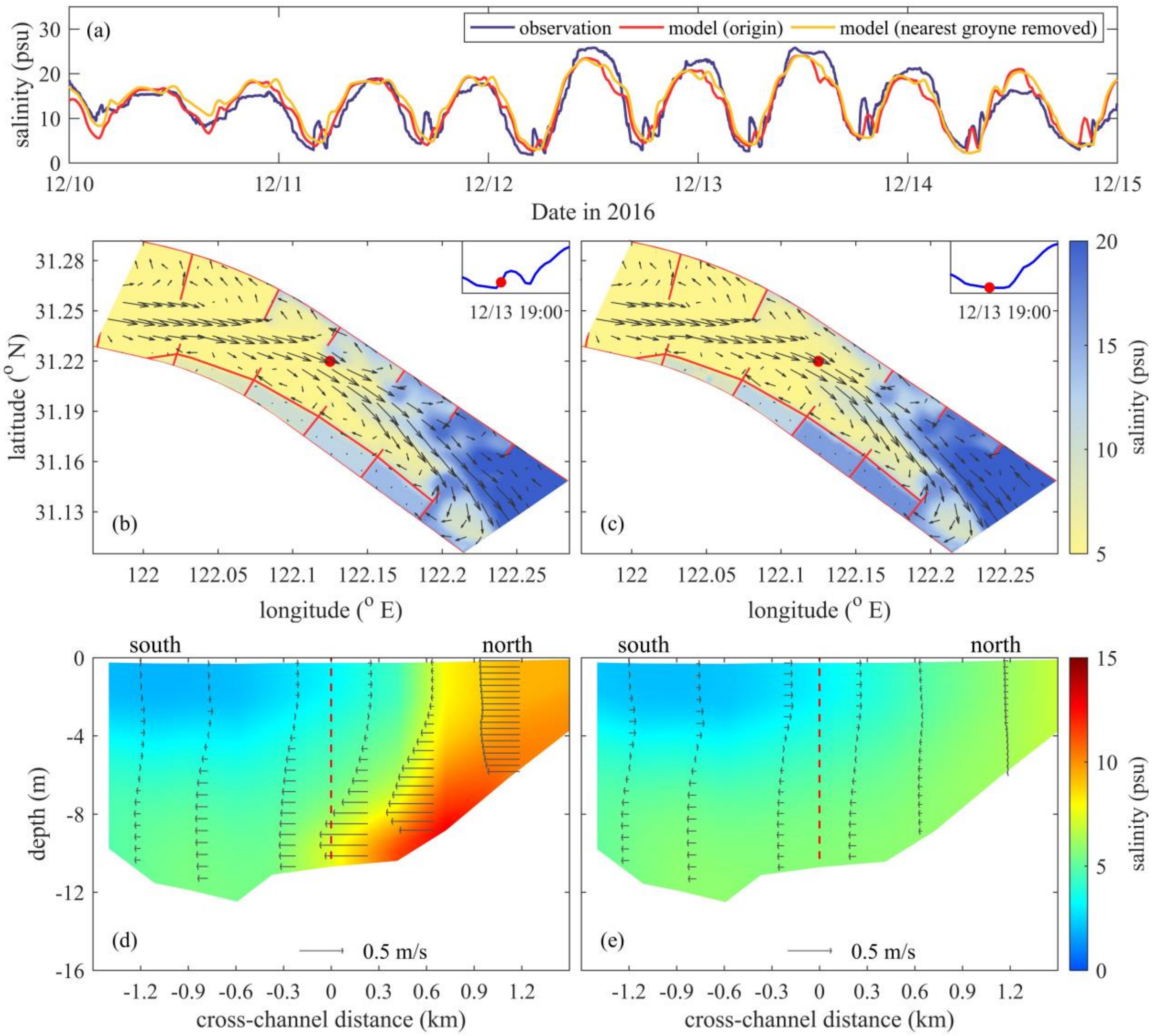

Figure 14: Model-data comparison with groyne-removed case added (a), comparison between original case (b, d) and groyne-removed case (c, e) at the same time in bottom salinity distribution (b, c) and vertical salinity distribution (d, e).

The numerical model results suggest that the groyne fields north of our observation site contribute much stronger to the generation of ISV's than their southern counterparts. Due to the retention effect all along the northern groynes lateral flows developed, and the salinity varied over the tidal cycle (Fig. 7). This was not true, however, for the south groynes. The southern groynes were connected by an additional along-estuary dike (Fig. 14b) which limited exchange flows between the groyne fields and the estuary. As a result, their salinity remained fairly constant in time (Fig. 7) and cross-channel flows did not develop from the south (Fig. 8).

The impact of groynes on lateral flows reported here has, to our knowledge, not been published elsewhere in the scientific literature, but constitutes an important contribution. Many researchers have reported groynes' impacts on flow hydrodynamics (Brevis et al., 2014; McCoy et al., 2008; Sukhodolov, 2014) and mass exchange (McCoy et al., 2007; Uijttewaal et al., 2001; Weitbrecht et al., 2008). These studies do not include salinity-induced density effect which is closely related to groynes. Groynes are used throughout the world to channelize flow, preventing siltation rates in fairways maintained to provide access to ships. Lateral flows may significantly contribute to near-bed sediment dynamics and siltation rates, and therefore resulting in the exact opposite effect they were originally designed for. As a result, comprehensive understanding of the impact of such engineering works are required for sustainable development of human-impacted estuaries.

4.4 Implications of ISV in other studies

Earlier studies in the North Passage of the Changjiang Estuary also identified the existence of ISV, but was not paid much attention to. Song et al. (2013) conducted a quadrapod observation at the slightly south of the deep channel. They observed a similar intra-tidal salinity variation during the low water slack (in their Fig. 2a). They used velocity skew and flux skewness to examine the lateral sediment transport, identified a net sediment transport from the south groyne to the deep channel with an opposite lateral transport from the north to the south side of the channel in near-bottom area (below 1 mab). This opposite lateral flow and the ISV was likely generated with the same mechanisms discussed in our study. We believe that the ISV in their study was also generated by saline water trapped in the north groyne-sheltered area as this saline water mass could move across the deep channel to where Song et al. (2013) conducted the observation. Actually, the ISV in their study should be a further dispersion of ISV generated from the north shoal and that is why the magnitude of ISV at their observation site was much weaker. The lateral flow discussed in our study should be taken into account when considering sediment transport in the North Passage, as its movement affects the whole deep channel in the cross-channel direction. This will improve the knowledge of severe siltation issues in the channel.

ISV was also detected in other estuaries. Ralston et al. (2012) deployed fixed instruments frame in the channel and on the shoal of Hudson River estuary, which also revealed clear evidence for ISV (in their Fig. 3a). The bottom salinity measured in the channel also varied within the tidal cycle during low water slack, and was also the result of lateral flows. They concluded their lateral flow was primarily related to topography features in a channel-shoal system. We believe that more estuaries and channels all over the world are characterized by lateral flows resulting in ISV's albeit that the responsible mechanism (in our case the baroclinic pressure gradient, in Ralston's case the topography) may differ.

The ISV directly gives a strong indication for lateral flows in a channel-shoal system. ISV can be a simple indicator of lateral flow and lateral processes which should be considered when investigating the hydrodynamics and sediment dynamics of estuaries with extensive shoals. Actually, the ISV is just one typical feature under the modulation of lateral flow. Besides, particular small-scale fluctuation in other variables (for example temperature) also occurs concurrently with ISV. Generally speaking, these small-scale fluctuations in multiple variables all indicate the importance of the lateral flow caused by many different reasons in a tidal channel-shoal system.

5 Conclusions

In this study, a tripod system integrated with multiple instruments was deployed in the North Passage of the Changjiang Estuary to measure lateral flow and its impacted salinity transport. Observation results revealed periodic formation of intra-tidal salinity variation during low water slack. The tripod observations indicated the intra-tidal salinity variation (ISV) was generated by a near-bed lateral flow from the shallow shoal to the deep channel. A high-resolution unstructured-grid model for the Changjiang Estuary has been applied to simulate this lateral flow and the salinity transport. The numerical simulation showed that the high-salinity water trapped over the shoal was transported to the deep channel during ebb tide. The momentum balance analysis based on model results identified the density-induced baroclinic pressure gradient was the dominant physical mechanism for the generation of this lateral flow. Cross-channel residual current had a consistent near-bed shoal-to-channel component, which was closely connected with the shoal-to-channel lateral flow. Salinity transport also showed a southward net transport pattern.

This mechanism produced intra-tidal peaks in salinity and influenced pattern of stratification and mixing in the cross-channel section. Strong stratification occurred with and enhanced by the lateral flow, which can potentially affect sediment behavior (for example hindered settling) and modulate the pattern of sediment transport.

The ISV can be a signal of active lateral process in a tidal estuary, especially in a human-impacted channel-shoal system. Our simulations show that dikes and groynes greatly influence the flow field in the channel and the retention effect of groynes predominantly contributes to this lateral flow. This conclusion reminds us of more caution when designing such engineering structures. The findings reported here provide a key element for future work on sedimentation issues in general, but in the North Passage in particular, since our work suggests that groynes generate a residual current directed from the shoals to the channel.

In particular, the role of salinity-induced currents on sediment dynamics as well as sediment-induced density effect on lateral flows needs to be further investigated. Since the results reported in this study were observed and simulated under dry-season freshwater discharge from the upstream Changjiang, caution should be taken when applying these results to wet season when freshwater discharge can be three to four times larger. Additional observations and model simulations are needed in that case.

Acknowledgments

This work is supported by the National Key R&D Program of China (Grant No.

2016YFA0600903), the NSFC project (Grant Nos. 41776104), and the KNAW project (Grant No. PSA-SA-E-02). All datasets used in this study are publicly available at https://figshare.com/s/d74327d26220f0802979.

Bowen, M. M. (2003). Salt transport and the time-dependent salt balance of a partially stratified estuary. *Journal of Geophysical Research*, *108*(C5), 3158. https://doi.org/10.1029/2001JC001231

Brevis, W., García-Villalba, M., & Niño, Y. (2014). Experimental and large eddy simulation study of the flow developed by a sequence of lateral obstacles. *Environmental Fluid Mechanics*, *14*(4), 873–893. https://doi.org/10.1007/s10652-013-9328-x

Chant, R. J. (2010). Estuarine secondary circulation. In A. Valle-Levinson (Ed.), *Contemporary Issues in Estuarine Physics* (pp. 100–124). Cambridge: Cambridge University Press. https://doi.org/DOI: 10.1017/CBO9780511676567.006

Chen, C., Liu, H., & Beardsley, R. C. (2003). An unstructured grid, finite-volume, three-dimensional, primitive equations ocean model: Application to coastal ocean and estuaries. *Journal of Atmospheric and Oceanic Technology*, *20*(1), 159–186. https://doi.org/10.1175/1520-0426(2003)020<0159:AUGFVT>2.0.CO;2

Chen, C., Beardsley, R., Cowles, G., Qi, J., Lai, Z., Gao, G., et al. (2013). An unstructured grid, Finite-Volume Coastal Ocean Model FVCOM -- User Manual. *Tech. Rep., SMAST/UMASSD-13-0701, Sch. for Mar. Sci. and Technol., Univ. of Mass. Dartmouth, New Bedford.*, *C*(July), 416 pp. https://doi.org/10.1017/CBO9781107415324.004

Dube, A., Jayaraman, G., & Rani, R. (2010). Modelling the effects of variable salinity on the temporal distribution of plankton in shallow coastal lagoons. *Journal of Hydro-Environment Research*, *4*(3), 199–209. https://doi.org/10.1016/j.jher.2010.03.003

Dyer, K. R. (1986). *Coastal and Estuarine Sediment Dynamics*. New York: John Wiley and Sons. Retrieved from https://books.google.nl/books?id=78kQAQAAIAAJ

Egbert, G. D., & Erofeeva, S. Y. (2002). Efficient inverse modeling of barotropic ocean tides. *Journal of Atmospheric and Oceanic Technology*, *19*(2), 183–204. https://doi.org/10.1175/1520-0426(2002)019<0183:EIMOBO>2.0.CO;2

Fischer, H. B. (1976). Mixing and Dispersion in Estuaries. *Annual Review of Fluid Mechanics*, *8*(1), 107–133. https://doi.org/10.1146/annurev.fl.08.010176.000543

Fugate, D. C., Friedrichs, C. T., & Sanford, L. P. (2007). Lateral dynamics and associated transport of sediment in the upper reaches of a partially mixed estuary, Chesapeake Bay, USA. Continental Shelf Research, 27(5), 679–698. https://doi.org/10.1016/j.csr.2006.11.012

Galperin, B., Kantha, L. H., Hassid, S., & Rosati, A. (1988). A Quasi-equilibrium Turbulent Energy Model for Geophysical Flows. *Journal of the Atmospheric Sciences*, *45*(1), 55–62. https://doi.org/10.1175/1520-0469(1988)045<0055:AQETEM>2.0.CO;2

Ge, J., Chen, C., Qi, J., Ding, P., & Beardsley, R. C. (2012). A dike–groyne algorithm in a terrain-following coordinate ocean model (FVCOM): Development, validation and application. *Ocean Modelling*, *47*, 26–40. https://doi.org/10.1016/j.ocemod.2012.01.006

Ge, J., Ding, P., Chen, C., Hu, S., Fu, G., & Wu, L. (2013). An integrated East China Sea-Changjiang Estuary model system with aim at resolving multi-scale regional-shelf-estuarine dynamics. *Ocean Dynamics*, *63*(8), 881–900. https://doi.org/10.1007/s10236-013-0631-3

Ge, J., Ding, P., & Chen, C. (2014). Low-salinity plume detachment under non-uniform summer wind off the Changjiang Estuary. *Estuarine, Coastal and Shelf Science*, *156*(1), 61–70. https://doi.org/10.1016/j.ecss.2014.10.012

Ge, J., Shen, F., Guo, W., Chen, C., & Ding, P. (2015). Estimation of critical shear stress for erosion in the Changjiang Estuary: A synergy research of observation, GOCI sensing and modeling. *Journal of Geophysical Research: Oceans*, *120*(12), 8439–8465. https://doi.org/10.1002/2015JC010992

Ge, J., Zhou, Z., Yang, W., Ding, P., Chen, C., Wang, Z. B., & Gu, J. (2018). Formation of Concentrated Benthic Suspension in a Time-Dependent Salt Wedge Estuary. *Journal of Geophysical Research: Oceans*. https://doi.org/10.1029/2018JC013876

Guo, W., Wang, X. H., Ding, P., Ge, J., & Song, D. (2018). A system shift in tidal choking due to the construction of Yangshan Harbour, Shanghai, China. *Estuarine, Coastal and Shelf Science*, *206*, 49–60. https://doi.org/10.1016/j.ecss.2017.03.017

Hoitink, A. J. F., van Maren, D. S., & Hoekstra, P. (2011). Mixing and stratification in a tropical tidal embayment subject to a distributed freshwater source. *Journal of Marine Systems*, *88*(1), 34–44. https://doi.org/10.1016/j.jmarsys.2011.02.015

Huijts, K. M. H., Schuttelaars, H. M., de Swart, H. E., & Valle-Levinson, A. (2006). Lateral entrapment of sediment in tidal estuaries: An idealized model study. Journal of Geophysical Research: Oceans, 111(12), 1–14. https://doi.org/10.1029/2006JC003615

Job Dronkers (2018): Estuarine circulation. Available from: http://www.coastalwiki.org/wiki/Estuarine_circulation [accessed on 29-04-2019]

Kim, Y. H., & Voulgaris, G. (2008). Lateral circulation and suspended sediment transport in a curved estuarine channel: Winyah Bay, SC, USA. *Journal of Geophysical Research: Oceans*, *113*(9), 1–15. https://doi.org/10.1029/2007JC004509

Lacy, J. R., & Sherwood, C. R. (2004). Accuracy of a pulse-coherent acoustic Doppler profiler in a wave-dominated flow. *Journal of Atmospheric and Oceanic Technology*, *21*(9), 1448–1461. https://doi.org/10.1175/1520-0426(2004)021<1448:AOAPAD>2.0.CO;2

Lai, Z., Chen, C., Cowles, G. W., & Beardsley, R. C. (2010). A nonhydrostatic version of FVCOM: 1. Validation experiments. *Journal of Geophysical Research: Oceans*, *115*(11). https://doi.org/10.1029/2009JC005525

Lerczak, J. A., & Rockwell Geyer, W. (2004). Modeling the Lateral Circulation in Straight, Stratified Estuaries*. *Journal of Physical Oceanography*, *34*(6), 1410–1428. https://doi.org/10.1175/1520-0485(2004)034<1410:MTLCIS>2.0.CO;2

Lewis, R., 1997. Dispersion in Estuaries and Coastal Waters. John Wiley & Sons Ltd.

Liu, G., Zhu, J., Wang, Y., Wu, H., & Wu, J. (2011). Tripod measured residual currents and sediment flux: Impacts on the silting of the Deepwater Navigation Channel in the Changjiang Estuary. *Estuarine, Coastal and Shelf Science*, *93*(3), 192–201. https://doi.org/10.1016/j.ecss.2010.08.008

McCoy, A., Constantinescu, G., & Weber, L. (2007). A numerical investigation of coherent structures and mass exchange processes in channel flow with two lateral submerged groynes. *Water Resources Research*, *43*(5), 1–26. https://doi.org/10.1029/2006WR005267

McCoy, A., Constantinescu, G., & Weber, L. J. (2008). Numerical Investigation of Flow Hydrodynamics in a Channel with a Series of Groynes. *Journal of Hydraulic Engineering*, *134*(2), 157–172. https://doi.org/10.1061/(asce)0733-9429(2008)134:2(157)

Mellor, G. L., & Yamada, T. (1982). Development of a turbulence closure model for geophysical fluid problems. *Reviews of Geophysics*, *20*(4), 851. https://doi.org/10.1029/RG020i004p00851

Nidzieko, N. J., Hench, J. L., & Monismith, S. G. (2009). Lateral Circulation in Well-Mixed and Stratified Estuarine Flows with Curvature. *Journal of Physical Oceanography*, *39*(4), 831–851. https://doi.org/10.1175/2008JPO4017.1

Postma, H. (1967). Sediment transport and sedimentation in the estuarine environment. In L. G.H (Ed.), *Eustuaries* (pp. 158–179). Washington DC. https://doi.org/10.4319/lo.1968.13.4.0725

Simpson, J. H., Brown, J., Matthews, J., & Allen, G. (1990). Tidal Straining, Density Currents, and Stirring in the Control of Estuarine Stratification. *Estuaries*, *13*(2), 125. https://doi.org/10.2307/1351581

Song, D., Wang, X. H., Cao, Z., & Guan, W. (2013). Suspended sediment transport in the Deepwater Navigation Channel, Yangtze River Estuary, China, in the dry season 2009: 1. Observations over spring and neap tidal cycles. *Journal of Geophysical Research: Oceans*, *118*(10), 5555–5567. https://doi.org/10.1002/jgrc.20410

Sukhodolov, A. N. (2014). Hydrodynamics of groyne fields in a straight river reach: Insight from field experiments. *Journal of Hydraulic Research*, *52*(1), 105–120. https://doi.org/10.1080/00221686.2014.880859

Uijttewaal, W. S. J., Lehmann, D., & Mazijk, A. Van. (2001). Exchange Processes between a River and Its Groyne Fields: Model Experiments. *Journal of Hydraulic Engineering*, *127*(11), 928–936. https://doi.org/10.1061/(ASCE)0733-9429(2001)127:11(928)

Wang, Z. B., Van Maren, D. S., Ding, P. X., Yang, S. L., Van Prooijen, B. C., De Vet, P. L. M., et al. (2015). Human impacts on morphodynamic thresholds in estuarine systems. *Continental Shelf Research*, *111*, 174–183. https://doi.org/10.1016/j.csr.2015.08.009

Weitbrecht, V., Socolofsky, S. A., & Jirka, G. H. (2008). Experiments on Mass Exchange between Groin Fields and Main Stream in Rivers. *Journal of Hydraulic Engineering*, *134*(2), 173–183. https://doi.org/10.1061/(asce)0733-9429(2008)134:2(173)

Woodroffe, C. D., Nicholls, R. J., Saito, Y., Chen, Z., & Goodbred, S. L. (2006). Landscape variability and the response of Asian megadeltas to environmental change. In *Global change and integrated coastal management* (pp. 277–314). Springer.

Wu, J., Liu, J. T., & Wang, X. (2012). Sediment trapping of turbidity maxima in the Changjiang Estuary. *Marine Geology*, *303–306*, 14–25. https://doi.org/10.1016/j.margeo.2012.02.011

Zhu, L., He, Q., & Shen, J. (2018). Modeling lateral circulation and its influence on the along-channel flow in a branched estuary. *Ocean Dynamics*, *68*(2), 177–191. https://doi.org/10.1007/s10236-017-1114-8